Iodine Migration and its Effect on Hysteresis in Perovskite Solar Cells

*Cheng Li, Steffen Tscheuschner, Fabian Paulus, Paul E. Hopkinson, Johannes Kießling, Anna Köhler, Yana Vaynzof, and Sven Huettner**

The past few years have witnessed a dramatic development of inorganic–organic halide organometal perovskite solar cells, which have captured the attention of the scientific community due to their high power conversion efficiencies[1] and simple fabrication processes.[2,3] Besides further improving the conversion efficiency[4] and stability,[5] important device related questions still need to be answered:[6,7] the hysteresis behavior, i.e., the discrepancy of the performance between two voltage-sweeping directions when performing a current–voltage (*J–V*) measurement. The possible origins include ferroelectricity,[8,9] low frequency capacitance,[10] trap states in the bulk,[11] interfacial dipoles,[12] as well as mobile ion screening.[13–15] Several groups have fabricated devices without significant hysteresis, for example, by using mesoporous TiO_2 layers instead of a compact TiO_2 layer,[16] solvent annealing to obtain large crystalline grains,[17] as well as a fullerene passivation method.[18]

Although there are several proposed mechanisms, recently more and more attention is focused on the role of ions/vacancies migration under an electrical field.[15,19–21] (1) The characterized decay time scale in perovskite solar cells is on a second timescale[22] (also see Figure S6, Supporting Information), while the ferroelectric domain polarization/depolarization process is much faster, in the picosecond range.[23,24] In addition, piezoresponse force microscopy[13,25] results also suggested that polarization switching in $CH_3NH_3PbI_3$ is unlikely to be the dominant reason for the hysteresis behavior. (2) By transient photovoltage and capacitance measurements, O'Regan et al.[26] proved that *J–V* curve hysteresis is not associated with the change of recombination rate and charge separation efficiency. (3) Simple trapping and detrapping of charges at defects in the bulk or at the interface is also unlikely to be the main mechanism due to the long duration and large magnitude of the current decay.[19] However, the trapping/detrapping process associated with migrating defects, such as iodine interstitials,[15,27] which can be driven by an electrical field, may play an important role in the hysteresis.

In brief, we used three different methods to reveal the underlying processes relating to hysteresis. First we employed electroabsorption (EA) spectroscopy, a noninvasive in situ characterization approach[28,29] to determine the built-in potential (V_{BI}) in solar cell devices. In a second experiment we applied a staircase voltage profile to these devices and measured the time dependent current at a series of temperatures in order to study the activation energy of the migrating species in perovskite based devices. In the last experiment we used X-ray photoemission spectroscopy (XPS) measurements to study the redistribution of elements within laterally configured devices after long-term electrical biasing. Our results suggest that the hysteresis in *J–V* curves originates from the interfacial barrier associated with the drift of iodide ions or the respective interstitial under an electrical field.

Figure 1a shows the scheme of a FTO/compact TiO_2/$CH_3NH_3PbI_{3-x}Cl_x$/Spiro-OMeTAD/Ag planar perovskite solar cell. As a p-i-n structure,[30,31] photogenerated electrons are collected by a FTO (fluorine doped tin oxide) electrode through a compact TiO_2 layer, and the holes by an Ag electrode through a layer of Spiro-OMeTAD (2,2′,7,7′-Tetrakis-(*N*,*N* -di-4-methoxyphenylamino)-9,9′-spirobifluorene), acting respectively as electron and hole transport layers (ETL/HTL). The ionization energy and the electron affinity of materials were estimated according to values reported in literature[1,14] and measurement of the optical bandgap (Figure S1, Supporting Information). The *J–V* curves of a $CH_3NH_3PbI_{3-x}Cl_x$ perovskite solar cell under AM 1.5G illumination in forward and reverse voltage sweeps are shown in Figure 1b. As shown in **Table 1**, there is a shift in V_{oc} of 0.22 V and a significant difference in the performance between the two sweeping directions. Note that the red dashed line depicts the extension of the *J–V* curve during

Dr. C. Li, J. Kießling, Prof. S. Huettner
Macromolecular Chemistry I
University of Bayreuth
Universitätstr. 30, 95447 Bayreuth, Germany
E-mail: sven.huettner@uni-bayreuth.de
S. Tscheuschner, Prof. A. Köhler
Experimental Physics II
University of Bayreuth
Universitätstr. 30, 95447 Bayreuth, Germany
F. Paulus
Organic Chemistry Institute
Im Neuenheimer Feld 270
Heidelberg University
69120 Heidelberg, Germany
Dr. P. E. Hopkinson, Prof. Y. Vaynzof
Kirchhof Institute for Physics
Im Neuenheimer Feld 227
Heidelberg University
69120 Heidelberg, Germany
Dr. P. E. Hopkinson, Prof. Y. Vaynzof
Centre for Advanced Materials
Im Neuenheimer Feld 225
Heidelberg University
69120 Heidelberg, Germany

DOI: 10.1002/adma.201503832

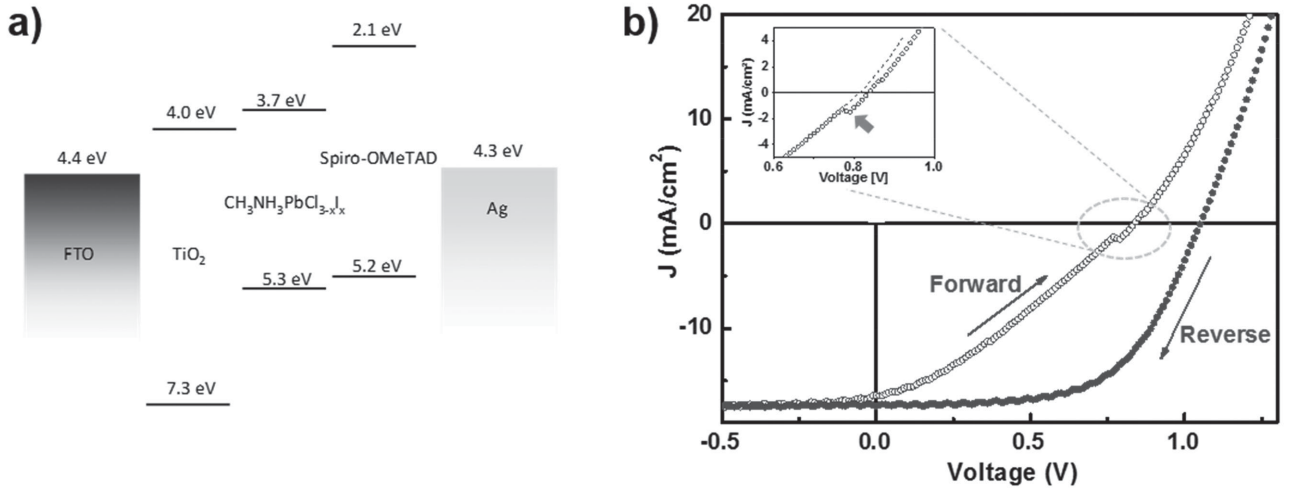

Figure 1. a) Energy diagram of a FTO/compact TiO_2/$CH_3NH_3PbI_{3-x}Cl_x$/Spiro-OMeTAD/Ag perovskite solar cell. b) Current–voltage (J–V) curve of a perovskite solar cell under AM 1.5G illumination. The arrows indicate the directions of applied external voltage (forward and reverse sweeping). Inset shows the kink in the J–V curve in detail. The dashed line is the extension of the J–V curve below ≈0.75 V, and the grey arrow indicates the shift of the curves near the flat-band condition. The scanning speed is 0.9 V s^{-1}.

the forward voltage sweep below 0.75 V, based on a single junction diode equation.[32] The inset in Figure 1b shows a magnification of the area around 0.75 V, and the shift of V_{oc} between the dashed extension line and the measured curve and the emerging kink will be discussed in the course of this work. This kink has been frequently observed in several papers, especially during fast scanning.[7,22,33] In addition, unlike the reverse sweep, in the forward sweep, the fill factor is significantly reduced and tends to look "S-curved" near V_{oc} implying that during forward sweeps there may exist injection barriers associated with interfacial dipoles at the perovskite/HTL or ETL interface,[34] or capacitive charging/discharging effects during the scanning process.[26,35]

To understand the origin of the hysteresis in $CH_3NH_3PbI_{3-x}Cl_x$ perovskite solar cells in more detail, we carried out the EA measurement in forward and reverse sweeping directions. We used an EA setup as described in detail in previous papers.[36,37] In brief, the absorption of materials can be modulated by an external electrical field due to the Stark effect. Here, a superposition of DC and AC voltages was applied to the device and the change in intensity of the reflective probe light, ΔR, was monitored by a silicon photodetector connected to a lock-in amplifier. According to the classical Stark effect theory,[38] the shift of the energy (ΔE) produced by the electrical field (F) arises from both the change of dipole moment ($\Delta\mu$) and polarizability (Δp)

$$\Delta E(F) \propto -\Delta\mu F - \frac{1}{2}F\Delta pF \tag{1}$$

Table 1. Device performance parameters of a FTO/compact TiO_2/$CH_3NH_3PbI_{3-x}Cl_x$/Spiro-OMeTAD/Ag perovskite solar cell, during the forward and reverse sweeping, respectively.

Sweep direction	J_{sc} [mA cm^{-2}]	V_{oc} [V]	FF [%]	PCE [%]
Forward	16.22	0.83	30.2	4.3
Reverse	17.62	1.05	60.1	12.0

The change in the absorption coefficient $\Delta\alpha$ or EA signal $\Delta R/R$, which is a function of ΔE, can be expressed by a Taylor expansion truncated by the quadratic term[39]

$$\Delta\alpha \propto \frac{\Delta R}{R} \propto \frac{\partial\alpha}{\partial E}\Delta E + \frac{1}{2}\frac{\partial^2\alpha}{\partial E^2}\Delta E^2 \tag{2}$$

By inserting Equation (1) into Equation (2), the lineshape of the EA spectrum can be regarded as a linear combination of the spectra resembling the first and second derivative of the unperturbed absorption spectrum. Two possible conditions can be considered:[38–40] (1) If there is no permanent dipole, i.e., only dipole moments induced by an external electrical field, the whole absorption spectrum will shift towards a lower energy. As a consequence, the change of absorption $\Delta\alpha$, or the EA spectrum $\Delta R/R$, exhibits a first derivative lineshape. (2) If permanent dipoles exist, $\Delta\mu F$ dominates Equation (2). Assuming $\Delta\mu > 0$, dipole moments that are aligned with the external electrical field will decrease in energy, while those aligned against the field will experience an increase in energy. As a result, the EA spectrum resembles a second derivative lineshape.

A typical EA spectrum of a $CH_3NH_3PbI_{3-x}Cl_x$ perovskite solar cell is shown in **Figure 2**, which overlaps well with the features of the second derivative of the unperturbed absorbance spectrum of the perovskite film. In addition, Wu et al.[28] have shown that these features are unaffected when using different ETL and HTL layers. This suggests that this EA response is mainly related to permanent dipoles within the bulk of the perovskite layer.

O'Regan et al.[26] proposed that the J–V curve hysteresis is ascribed to the band offset at the interface. Tress et al.[21] suggested that the hysteresis is due to the screening of build-in field by ionic migration, changing the effective difference in work functions of two contacts. Leguy et al.[24] proposed a similar decrease of work functions difference due to an alignment of ferroelectric domains. Therefore, to characterize the built-in potential within the device, we carried out DC dependent EA

DOI: 10.1002/adma.201503832

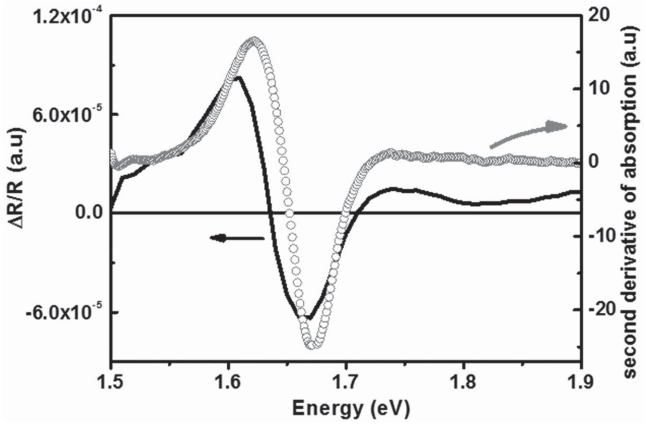

Figure 2. Comparison between EA spectrum of a $CH_3NH_3PbI_{3-x}Cl_x$ perovskite solar cell (black) and second derivative of $CH_3NH_3PbI_{3-x}Cl_x$ absorption spectrum (open symbols). Applied DC and AC voltage in EA measurement are –2 V and 1 V, respectively, and the AC frequency is 2.01 kHz.

measurements. The EA response ($\Delta R/R$) at the first harmonic of the applied AC bias is[37]

$$\left.\frac{\Delta R}{R}\right|_{\omega} \propto \chi(h\nu)V_0V_{AC}\sin(\omega t) = \chi(h\nu)(V_{DC}-V_{BI})V_{AC}\sin(\omega t) \quad (3)$$

Here, $\chi(h\nu)$ is the electric susceptibility of the materials, a function of the photon energy $h\nu$, while V_{DC} and V_{AC} are the applied external DC and AC voltages, respectively. V_{BI} is the built-in potential in the device and V_0 is the internal DC voltage. Based on the standard metal–insulator–metal model, the built-in potential V_{BI} relies on the work function difference between two electrodes.[41] Herein, according to Equation (3), V_{BI} can be determined by finding the nulling voltage V_{null} ($V_{null} = V_{DC} - V_{BI}$), when the EA signal is zero.

The spectra of the perovskite solar cell under a series of external DC voltages are shown in **Figure 3**a. The features of peaks located at 1.62 and 1.66 eV are nearly field-independent, while the amplitudes are proportional to the external DC voltage. In addition, at V_{DC} = 0 V an EA signal is still presented, indicating the nonzero built-in potential in the device. During the forward scan, from –2 to 0 V, the built-in potential is estimated as 1.0 ± 0.1 V (linear fit of 5 points at 1.66 eV in Figure 3a, indicated by the dashed line). Since the Spiro-OMeTAD is highly doped with a lithium salt, we can assume that the work function approaches the valance band (or highest occupied molecular orbital).[42] Therefore, the obtained V_{BI} can be regarded as approximately the work function difference between the TiO_2 and the Spiro-OMeTAD layer[3] which corresponds to a p-i-n structure as used in the theoretical description of EA.[13,36]

Figure 3b shows the DC dependent EA signal at a photon energy of 1.66 eV in forward and reverse sweeping direction, respectively. By sweeping from –2.5 to 2 V we obtain a V_{BI} = 1.0 ± 0.1 V, which is consistent with the spectra under a series of external DC voltages in Figure 3a. We notice that for voltages above +1 V, the EA signal exhibits a deviation from its linear relationship. This originates from the large charge injection and electroluminescence of this perovskite solar cell at higher positive voltages (Figure S5, Supporting Information). By reverse sweeping from 2 to –2.5 V, the device exhibits a V_{BI} of 1.3 ± 0.1 V, showing a shift of V_{BI} of 0.3 ± 0.1 V, reflecting the shift of V_{OC} as seen in Figure 1b. This reduction of V_{BI} is also consistent with the observation in rate-dependent J–V curve hysteresis measurement (Figure S3, Supporting Information).[21] This result implies a change of the effective work function of Spiro-OMeTAD and TiO_2 during sweeping. This change is shown in Figure S10 (Supporting Information) and can be caused by a modulation of the interfacial barrier.[43,44] In the negative voltage region, we notice that the EA response in the reverse curve (blue) deviates from a linear relationship, and the EA signal drops to near zero at ≈–1 V. We also observe that when applying larger negative voltages (greater than –3 V), both the forward and reverse curves merge (not shown here). We propose that this behavior is a further indication for ionic migration, i.e., the drift of ions within the bulk under a negative electrical field. This migration results in the redistribution of ions and disturbs the internal electrical

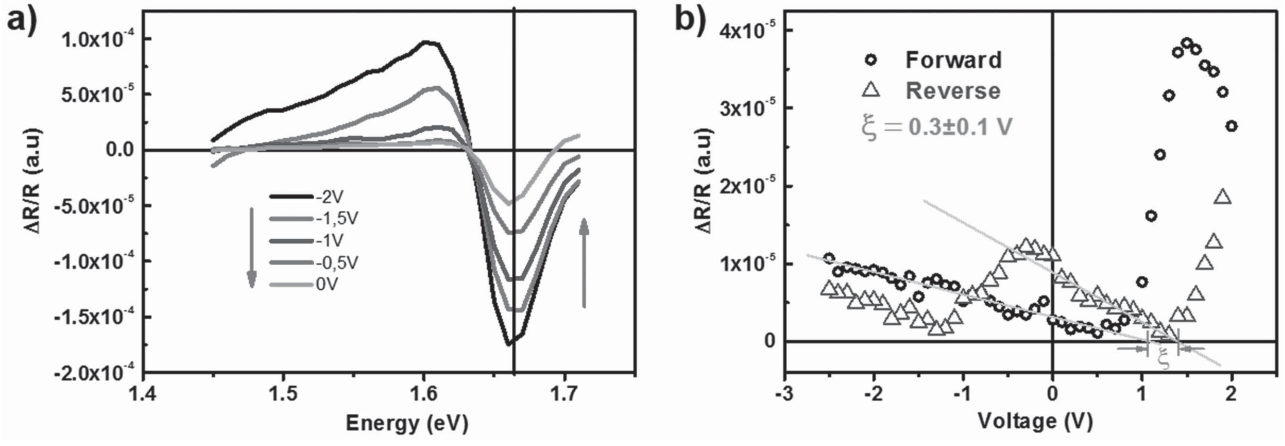

Figure 3. a) EA spectra of a perovskite solar cell under a series of DC voltages. The dashed line indicates the photon energy 1.66 eV selected for the DC voltage dependent EA characterization. The arrows show the order of applied external DC voltages. b) DC dependent EA signal at 1.66 eV, in the forward and reverse sweeping, respectively. Gray solid lines are linear fits of the EA signal to obtain the built-in potential. ξ is the shift of the built-in potential between forward and reverse sweeping directions. V_{AC} = 1 V, and AC frequency is 2.01 kHz. The FTO layer was grounded and the external voltage was applied to the Ag layer.

field, leading to the deviation of the standard EA signal.[45] This process is also time dependent and would automatically lead to a change of capacitance during the switching.[22,35]

Temperature dependent electrical measurements enable us to investigate the nature of the ionic species, such as the activation energy.[10,15,19,27,46,47] According to the chemical diffusion theory, if the transient curve fits an exponential behavior, it implies a chemical diffusion process is involved.[15,48] By applying subsequent voltage steps between –2 and 2 V, each step lasting for 40 s with an absolute step size of 0.5 V, we monitor the dynamic process of the electrical current response. As in a typical diode, the current densities in the negative voltage region are negligible (in both sweeping directions). In the positive region, time t dependent current density curves at different voltage steps can be fitted by a single exponential function $e^{-t/}\tau$ (Figure S7, Supporting Information). We observe that as the temperature decreases, the decay time increases, which is in good agreement with the observation in temperature dependent chronophotoamperometry measurement.[19] Therefore, this behavior is consistent with the chemical diffusion theory as mentioned above and suggests ions migration during the J–V curve measurement. In detail, Nian et al.[47] presented that the resistivity of perovskite materials exhibits an exponential relationship with the concentration of defects/ions at the interface. Even though the influence of diffusion and drift may be more complex, the good match with a monoexponential function suggests that we can assume a linear increase of the ion concentration with their migration velocity. Hence, the electrical current decay time τ can be considered to be proportional to the reciprocal of the velocity of ions.

We studied the decay time τ constant at 1.5 V, both in forward and reverse sweeping at different temperatures. **Figure 4**c,d plots $\ln(\tau)$ against $1000/T$ and within the margin of error, the curves between 200 and 300 K approximately show a straight line. The material undergoes a phase transition from a tetragonal to an orthorhombic phase[49] at ≈160 K, which is why the point at 150 K does not fit the same temperature dependency. This phase transition, has also been observed in temperature dependent capacitance measurement,[35] UV–vis absorbance spectra[50] and photoluminescence spectra.[51]

The movement of ions within the bulk of a material, especially in traditional perovskite materials (ABO_3), has been intensively investigated.[52] This linear relationship between $\ln(\tau)$ and $1/T$ suggests that the movement of ions is facilitated by a hopping mechanism among the atomic lattices under an external electrical field.[53] Vineyard presented an absolute rate theory in 1957, which describes an individual defect jump rate[53] of ions Γ in solids excited by thermal activation

$$\Gamma = \Gamma_0 e^{-\Delta E/k_B T} \tag{4}$$

Here, ΔE is the activation energy required to hop from one equilibrium site to the neighboring one, T is the absolute

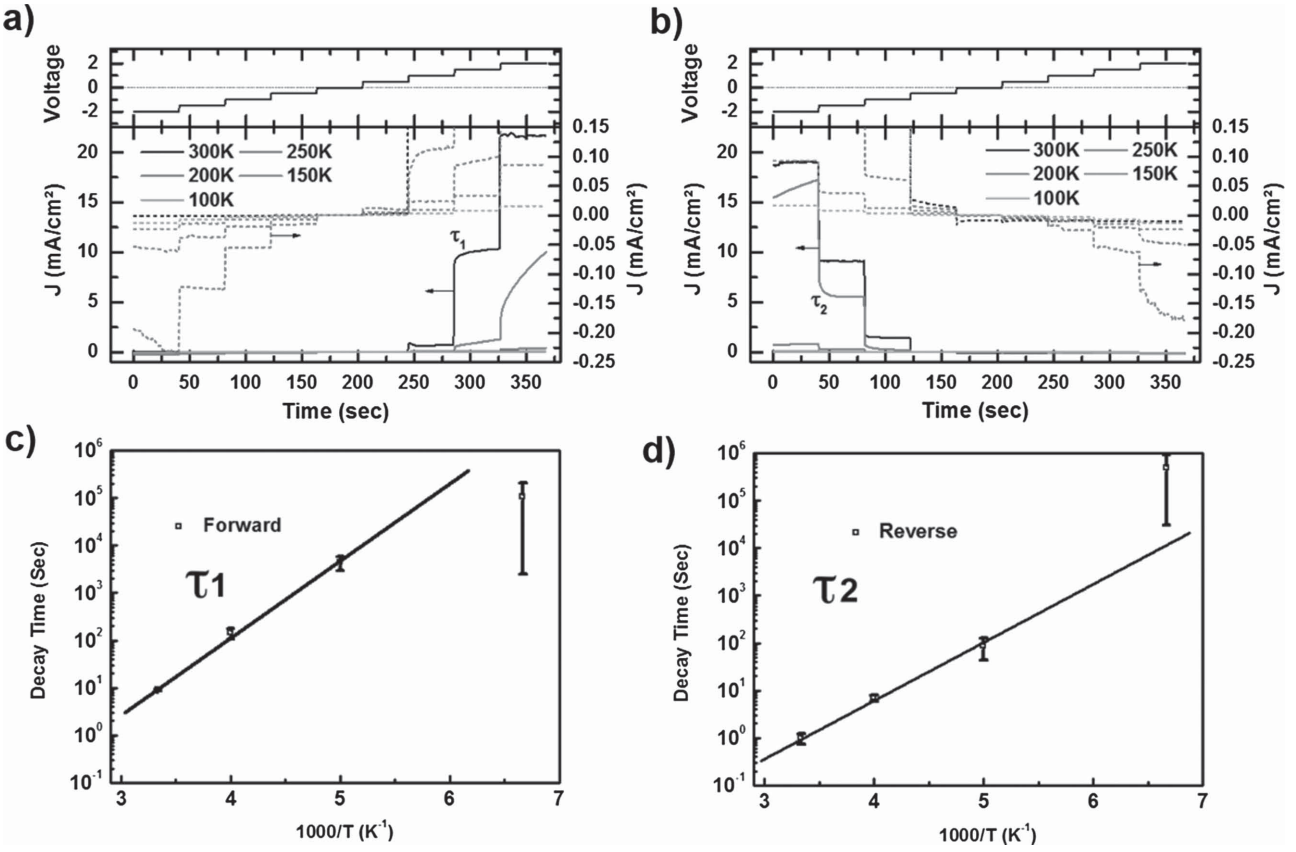

Figure 4. a,b) Temperature dependent current density against time curve of a perovskite solar cells in dark during the forward and reverse sweeping, respectively. c,d) The decay time τ at 1.5 V during forward and reverse sweeping against 1000/T, respectively. The solid lines are the linear fitting curves of first three points (300, 250, and 200 K).

Adv. Mater. **2016**,
DOI: 10.1002/adma.201503832

temperature, and k_B is the Boltzmann constant. Plotting $\ln(\tau)$ versus $1000/T$ (Figure 4c) generates a slope of $\Delta E/k_B = 3630$ K, resulting in a thermal activation energy of about 0.31 eV, while in Figure 4d the slope $\Delta E/k_B = 2659$ K, leads to an activation energy of about 0.23 eV. The discrepancy between these two activation energies may be ascribed to the concentration gradient of ions in the vicinity of the interfaces. These activation energies obtained are consistent with previous calculations between 0.16 and 0.33 eV.[20,54] We note that there are differences between our measurements and other reported results. Baumann et al.[55] obtained an activation energy through thermally stimulated current measurement around 0.5 eV. Eames et al.[19] found an activation energy around 0.6 eV through experimental and computational studies. Yang et al.[15] obtained an activation energy of 0.43 eV through temperature conductivity measurements. Almora et al.[35] calculated the activation energy of 0.45 eV by temperature dependent capacitance measurement. We propose that theses differences can be explained by the different fabrication methods used such as either long time annealing[15,19] or two-step fabrication,[55] which lead to different crystalline quality. Our extracted activation energies are very close to the lately reported theoretical calculations by Azpiroz et al.[20]and Haruyama et al.[54]

To study the redistribution of ions after long-term biasing, we used in a further experiment a lateral set of electrodes to apply a bias (**Figure 5**c) and subsequently analyzed the sample with XPS. XPS enables us to quantify the amount of a certain element in the vicinity of the surface. The I/Pb ratio in the as-prepared device between the two electrodes is ≈3.03, consistent with the stoichiometry of the perovskite materials. After biasing at 1 V for 30 min, the ratio of I/Pb becomes 5.65 ± 0.93 at the positive electrode and 2.29 ± 0.04 at the ground electrode (averaged over four separated pairs of electrodes).

In order to investigate the distribution of I and Pb ions between the electrodes (separated laterally by 200 µm as depicted in Figure 5 c), we measured the ratio of I/Pb at nine positions across the electrode pair after biasing at 1 V for 30 min (spot size ≈50 µm). At the positive electrode, in Figure 5f, the I/Pb ratio is 5.57, indicating an accumulation of I^- ions on that side. The ratio of I/Pb decreases across the electrode pair and at the negative electrode, the ratio of I/Pb is around 2.59, implying a lack of the iodide ions (or accumulation of iodide vacancies) there. After 6 h disconnection of the

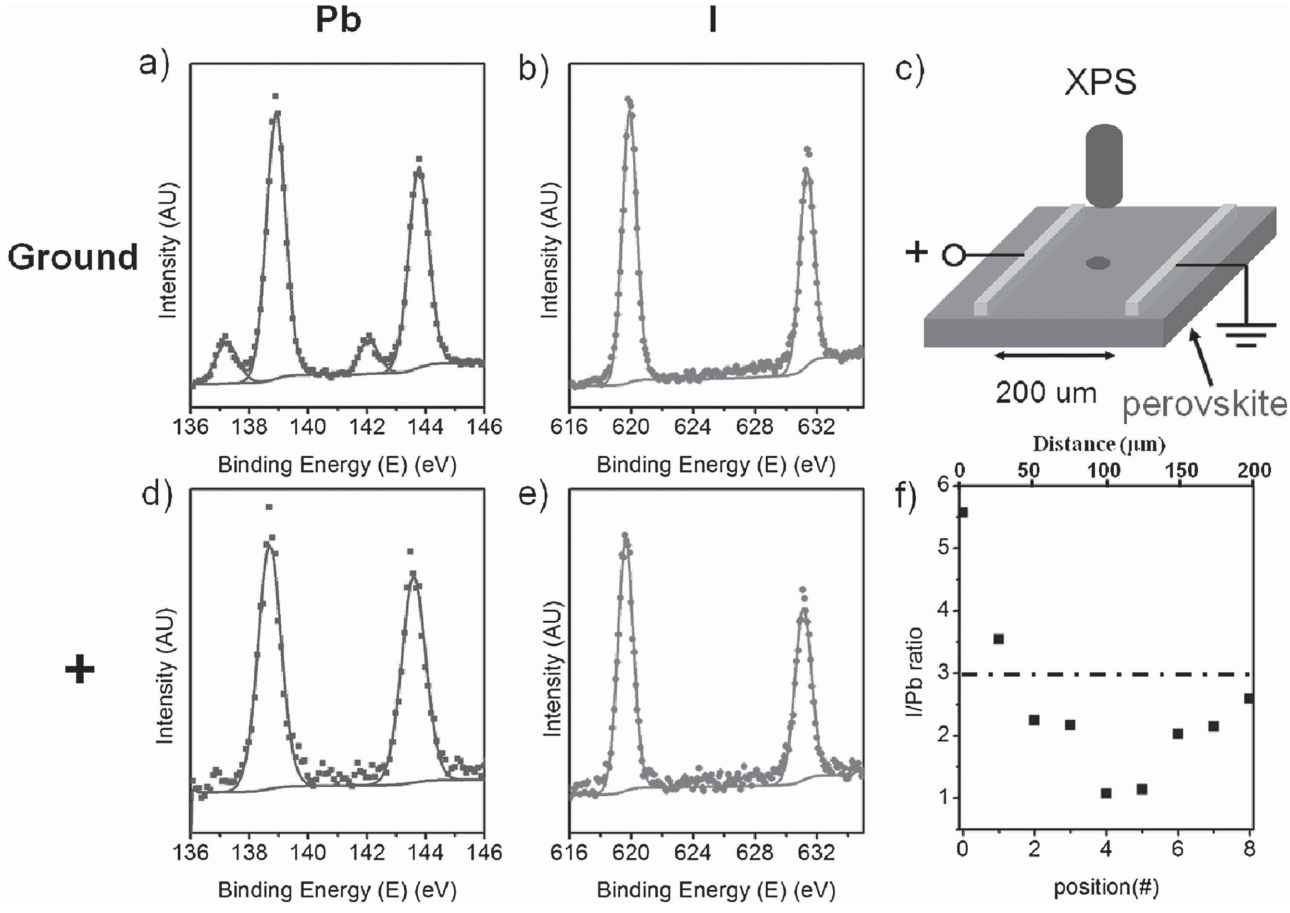

Figure 5. X-ray photoemission spectroscopy (XPS) result of a lateral $CH_3NH_3PbI_{3-x}Cl_x$ device. a,b) XPS spectra of Pb and I in the vicinity the ground electrode, respectively. d,e) The XPS spectra of Pb and I in the vicinity the positive electrode, respectively. c) Illustration of the set-up for characterization of elements distribution using a lateral structure. The applied DC voltage is 1 V for 30 min. The lateral distance between two electrodes is 200 µm. f) Distribution of the ratio of I/Pb between the electrode pairs after applying bias between two lateral electrodes. Position 0 is near the positive electrode and position 8 is near the ground electrode. The dashed line indicates the stoichiometry of perovskite, around 3.

external bias, the ratio of I/Pb at the positive electrode becomes ≈3 again (not shown here). Because the activation energy of Pb ions is very high, ≈2.31 eV,[19] we can assume that this change of I/Pb ratio is only due to the migration of iodide ions. Hence, this change of I/Pb ratio before and after biasing indicates that iodide ions can be driven by an external electrical bias, and these ions can diffuse back to the equilibrium states. This result is fitted nicely into the theoretical calculations of Duan et al.[27] and Azpiroz et al.,[20] in which the defect states in perovskite such as mobile iodide ions or iodine interstitials are the contributing species to the hysteretic behavior. Note that, as shown in Figure 5a, there are two sets of peaks for the Pb 4*f* visible in the XPS spectrum of Pb at the ground electrode and the ratio of I/Pb increases again. This suggests that a decomposition (i.e., electrochemical reaction) of the perovskite material under long term bias starts at this electrode (Figure S9, Supporting Information). A similar observation was recently reported by Fravola et al.[56] investigating the field-induced and photoinduced self-doping chemistry in perovskite films.[56] Kim et al.[57] proposed that the two sets of Pb 4*f* originate from the decomposition of the perovskite materials. Once iodine is no longer within the perovskite crystal structure, these iodide ions may not migrate under this electrical field, and leading to the increase of I/Pb ratio towards ≈3 near the ground electrode. In addition, the increase in the I/Pb ratio is also caused by the relatively large spot size (50 µm) of the XPS measurement.

The absence of hysteresis in FTO/TiO_2/Spiro-OMeTAD/Ag device, as shown in Figure S2 (Supporting Information), suggests that TiO_2 and Spiro-OMeTAD layers are not the main origin of hysteresis in perovskite solar cells. Several groups have proposed the energy band bending due to the migration of ions within the perovskite bulk.[19,21,58] Here, the results presented above suggest a mechanism for the hysteresis seen in perovskite solar cells during forward and reverse voltage sweeping. At the interfaces of $CH_3NH_3PbI_{3-x}Cl_x$ perovskite, two type-II heterojunctions are formed at the $CH_3NH_3PbI_{3-x}Cl_x$/TiO_2 and $CH_3NH_3PbI_{3-x}Cl_x$/Spiro-OMeTAD interfaces, respectively.[3,12] We can assume that due to the high doping level in the Spiro-OMeTAD layer,[42] the Fermi level of TiO_2 is approaching its conduction band (Figure S2, Supporting Information) and relatively high conductivity of TiO_2 layer (Figure S4, Supporting Information), the band bending in both layers is negligible as illustrated in the energy diagram in **Figure 6**a. Furthermore, V_{BI} measured in EA measurement is determined in the reversed bias region, as shown in Figure 3b, in which the overall current is small. In this respect, the perovskite solar cell can be considered as a multilayer capacitor, and TiO_2 layer serves as a dielectric layer in series with the perovskite layer. The dielectric constant of TiO_2, around 100,[59] is much higher than the one of perovskite materials, which is between 18 and 36.[9,35,60] Concerning the thickness of TiO_2 (≈50 nm) and perovskite (≈400 nm), most of the voltage drops within the perovskite layer in the reversed bias region. This has been observed, for example, using Kelvin probe force microscopy by mapping the potential distribution in the perovskite solar cells.[31]

When a positive bias is applied at the Spiro-OMeTAD layer while the TiO_2 layer is grounded, iodide ions I^- are driven towards the $CH_3NH_3PbI_{3-x}Cl_x$/Spiro-OMeTAD interface, leaving iodine vacancies at the opposite electrode. These changes lead to band bending within the $CH_3NH_3PbI_{3-x}Cl_x$ layer in the proximity of the two interfaces as shown in Figure 6b. In this case, the electron and hole injection/extraction improves by tunneling through these narrow interfacial barriers.[44] Thus positive charges accumulate at the TiO_2/perovskite interface and cause compensating negative charges to accumulate at the TiO_2 layer resulting in an upshift of the effective work function of TiO_2 (the Fermi level moves towards the vacuum level). The same happens at the Spiro-OMeTAD layer, with the only difference that the work function shifts downwards (the Fermi level moves away from the vacuum level).[44] Consequently, the built-in potential (which originates from the effective work function difference between the p- and n-type collection layers) experiences an increase with a concomitant decrease of the local injection barriers at these interfaces due to local band bending (Figure S10, Supporting Information). In addition, bimolecular recombination, which is strongly related with the built-in field in the bulk will also significantly decrease.[36,61] This results in an increase of open circuit voltage V_{oc} and enhancement of the device performance, as illustrated in Figure 1b.

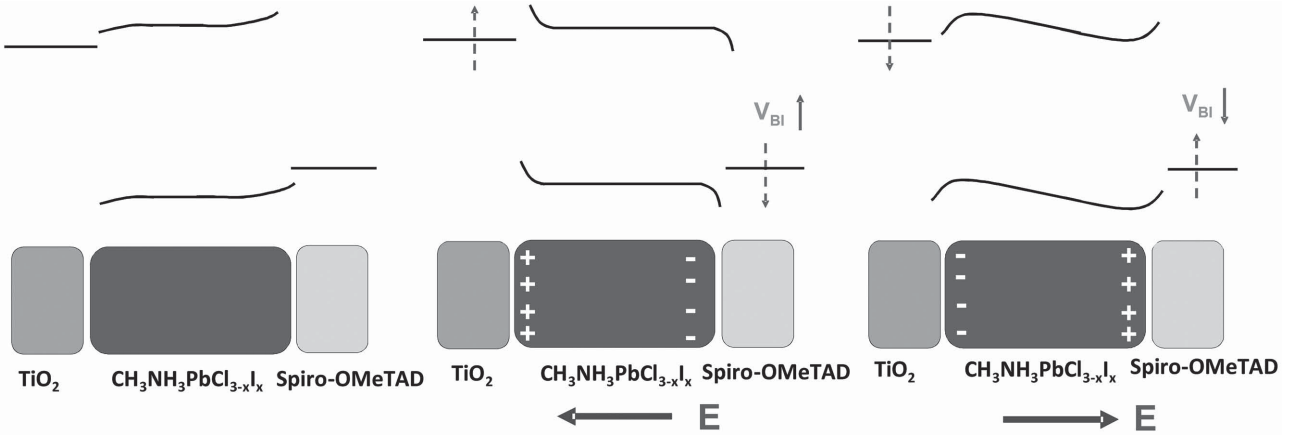

Figure 6. Schematic diagrams of band bending in the perovskite solar cells under electrical fields. The dashed arrows indicate the direction of the effective work function movement. *E* presents the direction of the external electrical field.

Adv. Mater. **2016**,
DOI: 10.1002/adma.201503832

Conversely, when applying a negative bias to the Spiro-OMeTAD layer, negatively charged iodide ions, are driven towards the perovskite/TiO_2 interface. In this respect, this change in the distribution of iodide ions alters the band alignment as shown in Figure 6c, resulting in the formation of larger injection barriers at the two perovskite interfaces. These two interfaces hinder the charge injection/extraction due to the formation of interfacial barriers. In addition, the accumulated ions effectively shift down the work function of TiO_2 and shifts up that of the Spiro-OMeTAD, causing a decrease of both the effective built-in potential and the open circuit voltage.

We can now give an explanation for the kink in the *J–V* curve as shown in Figure 1b (indicated by the blue circle) which is usually visible in forward sweeping[7] (and of course depends on the scanning speed). Coming from a negative bias the flat band condition is reached at this point. No electrical field is prevalent at this stage and ion diffusion (no drift) rearranges the built-in potential, which in return shifts V_{oc}.

The presented results imply that improving the crystallinity and quality of the perovskite layer may significantly reduce the density of mobile ions, thereby decreasing the hysteretic behavior. This is consistent with recently reported methods using solvent annealing or mesoporous TiO_2 layers.[16,17]

With these results we can give a concise interpretation of the ion migration, which is dominated by iodide ions. We note that the complete picture of ion movement might be much more complicated due to the coupling between charge transport and ion migration, strong spin–orbit coupling and atomic lattice distortions.[62] The accumulation of ions at the interfaces might further enhance the generation of local defects/interstitials in the lattice, resulting in an enhancement of ions movement through drift and diffusion.[63] In addition, the polycrystalline structure of the perovskite film can also complicate the mechanism owing to complex boundary conditions.[64] In this work, we cannot absolutely rule out the contribution of ferroelectricity of perovskites on the hysteresis, it may play a minor role on the behavior and has not been observed thus far. Methylammonium ions may have to be considered as well[11,12,20] and are subject of further investigation, however, our results clearly show that the migration of iodine plays the major role.

In this article, we investigated the mechanism that mainly contributes to the hysteresis in planar FTO/compact TiO_2/$CH_3NH_3PbI_{3-x}Cl_x$/Spiro-OMeTAD/Ag perovskite solar cells. Through DC dependent EA spectra, temperature dependent electrical measurement and XPS characterization, we can attribute the hysteresis to the modulation of interfacial barriers at $CH_3NH_3PbI_{3-x}Cl_x$/Spiro-OMeTAD and TiO_2/$CH_3NH_3PbI_{3-x}Cl_x$. This modulation is caused by the migration of iodide ions/interstitials driven by an external electrical bias leading to shift in the effective work function at the respective electrodes. By removing these defects related ions, it is likely that we can further enhance the solar cells performance and decrease the hysteretic behaviors. This investigation should contribute to the fundamental understanding of hybrid organic–inorganic material, paving the path for their further development and large-scale industrial application.

Experimental Section

Spiro-OMeTAD was purchased from Merck company, all the other chemicals were purchased from Sigma-Aldrich and were used as received.

Preparation of $CH_3NH_3PbI_{3-x}Cl_x$ Precursor: CH_3NH_3I was synthesized at room temperature for 2.5 h by reacting methylamine (CH_3NH_2, 33 wt% in ethanol) and hydroiodic acide (HI, 57 wt% in water with stabilizer). The ethanol was removed by a rotary evaporator, and the white powder was washed with diethyl ether. Then the product was further dried on hotplate at 70°C and stored in a nitrogen glovebox.

$CH_3NH_3PbI_{3-x}Cl_x$ Perovskite Solar Cells Fabrication and J–V Curve Characterization: Fluorine-doped tin oxide (F:SnO_2) coated glass was patterned by Zn power and HCl solution. FTO glasses were washed successively with acetone, 2% hellmanex diluted in deionized water, deionized water, and isopropanol for 10 min each. A compact TiO_2 layer was deposited by spraying a solution of titanium diisopropoxide bis(acetylacetonate) (0.6 mL) in ethanol (21.4 mL) at 450 °C for 90 min in ambient atmosphere. CH_3NH_3I and lead chloride ($PbCl_2$) were dissolved in anhydrous *N*,*N*-dimethylformamide at 3:1 molar ratio to make a mixture. This perovskite solution was spin-coated at 2000 rpm for 60 s. After drying in a nitrogen glovebox for ≈30 min, the as-spun films were annealed at 100 °C for 90 min. Spiro-OMeTAD solution was prepared by dissolving 72.3 mg Spiro-OMeTAD, 26.3 µL lithium-bis(trifluoromethanesulfonyl)imide (Li-TFSI) solution (520 mg Li-TFSI in 1 mL acetonitrile), and 43.2 µL 4-tert-butylpyridine in 1 mL chlorobenzene. This hole transport layer was deposited by spin-coating at 4000 rpm for 30 s. All device fabrication steps were carried out within a nitrogen filled glovebox. Finally, a 150 nm silver electrode was deposited by thermal evaporation in a chamber with a pressure of 1×10^{-6} mbar. The effective electrode area was 9 mm^2 or 16 mm^2.

J–V measurements were performed under inert environment with a Keithley 2400 source measure unit under 100 mW cm^{-2} illumination from an AM 1.5 solar simulator. The active area of 4 and 9 mm^2 were defined by the overlap of a black mask aperture area, the FTO and the evaporated top electrode. The light intensity was calibrated before by a Si detector. There was no biasing process prior the scanning, we scanned from 2 to −1 V and then measured the reverse scanning continuously. The delay time was 0.01, 0.05, 0.1, and 1 s, respectively. During the delay time, the voltage was kept constant. The step was 0.01 V. Number of power line cycles (NPLC) was 0.1.

EA Characterization: The light source was installed within a monochromator illuminator (Oriel Company). The light going through the monochromator (SPEX 1681B, Horiba Scientific) illuminated the device and was reflected back from the silver electrode onto a photodiode (HUV-4000B, EG&G Judson). A dual channel lock-in amplifier (SR 830 from Stanford Research Systems) was used to bias the device with a DC and an AC voltage and monitored the AC amplitude of the EA signal from the photodiode. In parallel the DC amplitude of the EA signal was recorded with a digital multimeter (HP34401A). For all the electrical experiment, the FTO electrode was connected to the ground, and Ag electrode was applied external voltages.

XPS Experiment: Heavily doped silicon substrates with a 300 nm oxide layer were cleaned successively with acetone, deionized water, and isopropanol for 10 min each in an ultrasonic bath. Then CH_3NH_3I and lead chloride ($PbCl_2$) were dissolved in anhydrous *N*,*N*-dimethylformamide at 3:1 molar ratio. This perovskite solution was spin-coated at 3000 rpm for 60 s. After drying in a nitrogen glovebox for ≈30 min, the as-spun films were annealed at 100 °C in a glovebox for 90 min. Finally, the devices were transferred into an evaporation chamber, and 150 nm of silver was deposited by thermal evaporation through a shadow mask within a chamber pressure of 1×10^{-6} mbar. The electrode distance was 200 µm and the interdigitating electrode geometry provided a ratio between width *W* and length, *W*/*L* of 500. A bias was applied to the devices in a nitrogen glovebox.

The samples were then transferred to the ultrahigh vacuum chamber of the Thermo Scientific ESCALAB 250Xi XPS system. The XPS measurements were carried out using a XR6 monochromated Al k_α

source ($h\nu$ = 1486.6 eV) using a 50 µm spot size. The measurements were collected between the Ag electrodes in steps of 30 µm.

Supporting Information

Supporting Information is available from the Wiley Online Library or from the author.

Acknowledgements

The authors gratefully acknowledge the financial support from the Bavarian frame work program Solar Technologies Go Hybrid. The authors are grateful to Fabian Panzer, Tanaji Gujar and Thomas Unger for valuable discussions.

Received: August 6, 2015
Revised: October 2, 2015
Published online:

[1] H. Zhou, Q. Chen, G. Li, S. Luo, T. B. Song, H. S. Duan, Z. Hong, J. You, Y. Liu, Y. Yang, *Science* **2014**, *345*, 542.
[2] J. Burschka, N. Pellet, S.-J. Moon, R. Humphry-Baker, P. Gao, M. K. Nazeeruddin, M. Grätzel, *Nature* **2013**, *499*, 316.
[3] M. A. Green, A. Ho-Baillie, H. J. Snaith, *Nat. Photonics* **2014**, *8*, 506.
[4] N. J. Jeon, J. H. Noh, W. S. Yang, Y. C. Kim, S. Ryu, J. Seo, S. I. Seok, *Nature* **2015**, *517*, 476.
[5] a) G. Niu, X. Guo, L. Wang, *J. Mater. Chem. A* **2015**, *3*, 8970; b) C.-C. Chueh, C.-Z. Li, A. K. Y. Jen, *Energy Environ. Sci.* **2015**, *8*, 1160.
[6] a) M. D. McGehee, *Nat. Mater.* **2014**, *13*, 845; b) E. L. Unger, E. T. Hoke, C. D. Bailie, W. H. Nguyen, A. R. Bowring, T. Heumuller, M. G. Christoforo, M. D. McGehee, *Energy Environ. Sci.* **2014**, *7*, 3690.
[7] H. J. Snaith, A. Abate, J. M. Ball, G. E. Eperon, T. Leijtens, N. K. Noel, S. D. Stranks, J. T.-W. Wang, K. Wojciechowski, W. Zhang, *J. Phys. Chem. Lett.* **2014**, *5*, 1511.
[8] J. M. Frost, K. T. Butler, F. Brivio, C. H. Hendon, M. Van Schilfgaarde, A. Walsh, *Nano Lett.* **2014**, *14*, 2584.
[9] J. M. Frost, K. T. Butler, A. Walsh, *APL Mater.* **2014**, *2*, 081506.
[10] H. S. Kim, N.-G. Park, *J. Phys. Chem. Lett.* **2014**, *5*, 2927.
[11] X. Wu, M. T. Trinh, D. Niesner, H. Zhu, Z. Norman, J. S. Owen, O. Yaffe, B. J. Kudisch, X.-Y. Zhu, *J. Am. Chem. Soc.* **2015**, *137*, 2089.
[12] G. Xing, B. Wu, S. Chen, J. Chua, N. Yantara, S. Mhaisalkar, N. Mathews, T. C. Sum, *Small* **2015**, *11*, 3606.
[13] Z. Xiao, Y. Yuan, Y. Shao, Q. Wang, Q. Dong, C. Bi, P. Sharma, A. Gruverman, J. Huang, *Nat. Mater.* **2015**, *14*, 193.
[14] Z.-K. Tan, R. S. Moghaddam, M. L. Lai, P. Docampo, R. Higler, F. Deschler, M. Price, A. Sadhanala, L. M. Pazos, D. Credgington, F. Hanusch, T. Bein, H. J. Snaith, R. H. Friend, *Nat. Nanotechnol.* **2014**, *9*, 687.
[15] T.-Y. Yang, G. Gregori, N. Pellet, M. Grätzel, J. Maier, *Angew. Chem. Int. Ed.* **2015**, *54*, 7905.
[16] N. J. Jeon, J. H. Noh, Y. C. Kim, W. S. Yang, S. Ryu, S. I. Seok, *Nat. Mater.* **2014**, *13*, 897.
[17] W. Nie, H. Tsai, R. Asadpour, A. J. Neukirch, G. Gupta, J. J. Crochet, M. Chhowalla, S. Tretiak, M. A. Alam, H.-L. Wang, *Science* **2015**, *347*, 522.
[18] Y. Shao, Z. Xiao, C. Bi, Y. Yuan, J. Huang, *Nat. Commun.* **2014**, *5*, 5784.
[19] C. Eames, J. M. Frost, P. R. F. Barnes, B. C. O'Regan, A. Walsh, M. S. Islam, *Nat. Commun.* **2015**, *6*, 7497.
[20] J. M. Azpiroz, E. Mosconi, J. Bisquert, F. De Angelis, *Energy Environ. Sci.* **2015**, *8*, 2118.
[21] W. Tress, N. Marinova, T. Moehl, S. M. Zakeeruddin, M. K. Nazeeruddin, M. Gratzel, *Energy. Environ. Sci.* **2015**, *8*, 995.
[22] R. S. Sanchez, V. Gonzalez-Pedro, J.-W. Lee, N.-G. Park, Y. S. Kang, I. Mora-Sero, J. Bisquert, *J. Phys. Chem. Lett.* **2014**, *5*, 2357.
[23] J. M. Frost, K. T. Butler, A. Walsh, *APL Mater.* **2014**, *2*, 081506.
[24] A. M. A. Leguy, J. M. Frost, A. P. McMahon, V. G. Sakai, W. Kockelmann, C. Law, X. Li, F. Foglia, A. Walsh, B. C. O'Regan, J. Nelson, J. T. Cabral, P. R. F. Barnes, *Nat. Commun.* **2015**, *6*, 7124.
[25] Z. Fan, J. Xiao, K. Sun, L. Chen, Y. Hu, J. Ouyang, K. P. Ong, K. Zeng, J. Wang, *J. Phys. Chem. Lett.* **2015**, *6*, 1155.
[26] B. C. O'Regan, P. R. F. Barnes, X. Li, C. Law, E. Palomares, J. M. Marin-Beloqui, *J. Am. Chem. Soc.* **2015**, *137*, 5087.
[27] H.-S. Duan, H. Zhou, Q. Chen, P. Sun, S. Luo, T.-B. Song, B. Bob, Y. Yang, *Phys. Chem. Chem. Phys.* **2015**, *17*, 112.
[28] X. Wu, H. Yu, L. Li, F. Wang, H. Xu, N. Zhao, *J. Phys. Chem. C* **2015**, *119*, 1253.
[29] V. Roiati, E. Mosconi, A. Listorti, S. Colella, G. Gigli, F. De Angelis, *Nano Lett.* **2014**, *14*, 2168.
[30] H. A. Abbas, R. Kottokkaran, B. Ganapathy, M. Samiee, L. Zhang, A. Kitahara, M. Noack, V. L. Dalal, *APL Mater.* **2015**, *3*, 016105.
[31] V. W. Bergmann, S. A. L. Weber, F. Javier Ramos, M. K. Nazeeruddin, M. Grätzel, D. Li, A. L. Domanski, I. Lieberwirth, S. Ahmad, R. Berger, *Nat. Commun.* **2014**, *5*, 5001.
[32] a) J. You, Y. M. Yang, Z. Hong, T.-B. Song, L. Meng, Y. Liu, C. Jiang, H. Zhou, W.-H. Chang, G. Li, Y. Yang, *Appl. Phys. Lett.* **2014**, *105*, 183902; b) J.-H. Im, I.-H. Jang, N. Pellet, M. Grätzel, N.-G. Park, *Nat. Nanotechnol.* **2014**, *9*, 927.
[33] a) D. A. Egger, E. Edri, D. Cahen, G. Hodes, *J. Phys. Chem. Lett.* **2015**, *6*, 279; b) J. Wei, Y. Zhao, H. Li, G. Li, J. Pan, D. Xu, Q. Zhao, D. Yu, *J. Phys. Chem. Lett.* **2014**, *5*, 3937; c) B. Wu, K. Fu, N. Yantara, G. Xing, S. Sun, T. C. Sum, N. Mathews, *Adv. Energy Mater.* **2015**, *5*, 1500829.
[34] A. Kumar, S. Sista, Y. Yang, *J. Appl. Phys.* **2009**, *105*, 094512.
[35] O. Almora, I. Zarazua, E. Mas-Marza, I. Mora-Sero, J. Bisquert, G. Garcia-Belmonte, *J. Phys. Chem. Lett.* **2015**, *6*, 1645.
[36] C. Li, D. Credgington, D.-H. Ko, Z. Rong, J. Wang, N. C. Greenham, *Phys. Chem. Chem. Phys.* **2014**, *16*, 12131.
[37] T. M. Brown, R. H. Friend, I. S. Millard, D. J. Lacey, T. Butler, J. H. Burroughes, F. Cacialli, *J. Appl. Phys.* **2003**, *93*, 6159.
[38] G. U. Bublitz, S. G. Boxer, *Annu. Rev. Phys. Chem.* **1997**, *48*, 213.
[39] L. Sebastian, G. Weiser, H. Bässler, *Chem. Phys.* **1981**, *61*, 125.
[40] F. W. Vance, R. D. Williams, J. T. Hupp, *Int. Rev. Phys. Chem.* **1998**, *17*, 307.
[41] I. H. Campbell, T. W. Hagler, D. I. Smith, J. P. Ferraris, *Phys. Rev. Lett.* **1996**, *76*, 1900.
[42] R. Schölin, M. H. Karlsson, S. K. Eriksson, H. Siegbahn, E. M. J. Johansson, H. Rensmo, *J. Phys. Chem. C* **2012**, *116*, 26300.
[43] C. Li, G. J. Beirne, G. Kamita, G. Lakhwani, J. Wang, N. C. Greenham, *J. Appl. Phys.* **2014**, *116*, 114501.
[44] I. H. Campbell, B. K. Crone, *Appl. Phys. Lett.* **2006**, *88*, 172113.
[45] J. C. De Mello, N. Tessler, S. C. Graham, R. H. Friend, *Phys. Rev. B* **1998**, *57*, 12951.
[46] L. K. Ono, S. R. Raga, S. Wang, Y. Kato, Y. Qi, *J. Mater. Chem. A* **2015**, *3*, 9074.
[47] Y. B. Nian, J. Strozier, N. J. Wu, X. Chen, A. Ignatiev, *Phys. Rev. Lett.* **2007**, *98*, 146403.
[48] I. Yokota, *J. Phys. Soc. Jpn.* **1961**, *16*, 2213.
[49] a) H.-S. Kim, S. H. Im, N.-G. Park, *J. Phys. Chem. C* **2014**, *118*, 5615; b) A. Poglitsch, D. Weber, *J. Chem. Phys.* **1987**, *87*, 6373.
[50] V. D'Innocenzo, G. Grancini, M. J. P. Alcocer, A. R. S. Kandada, S. D. Stranks, M. M. Lee, G. Lanzani, H. J. Snaith, A. Petrozza, *Nat. Commun.* **2014**, *5*, 3586.

[51] H.-H. Fang, R. Raissa, M. Abdu-Aguye, S. Adjokatse, G. R. Blake, J. Even, M. A. Loi, *Adv. Funct. Mater.* **2015**, *25*, 2378.
[52] M. B. Salamon, M. Jaime, *Rev. Mod. Phys.* **2001**, *73*, 583.
[53] G. H. Vineyard, *J. Phys. Chem. Solids* **1957**, *3*, 121.
[54] J. Haruyama, K. Sodeyama, L. Han, Y. Tateyama, *J. Am. Chem. Soc.* **2015**, *137*, 10048.
[55] A. Baumann, S. Väth, P. Rieder, M. C. Heiber, K. Tvingstedt, V. Dyakonov, *J. Phys. Chem. Lett.* **2015**, *6*, 2350.
[56] L. A. Frolova, N. N. Dremova, P. A. Troshin, *Chem. Commun.* **2015**, *51*, 14917.
[57] Y.-H. Kim, H. Cho, J. H. Heo, T.-S. Kim, N. Myoung, C.-L. Lee, S. H. Im, T.-W. Lee, *Adv. Mater.* **2015**, *27*, 1248.
[58] Y. Zhao, C. Liang, H. Zhang, D. Li, D. Tian, G. Li, X. Jing, W. Zhang, W. Xiao, Q. Liu, F. Zhang, Z. He, *Energy Environ. Sci.* **2015**, *8*, 1256.
[59] R. A. Parker, *Phys. Rev.* **1961**, *124*, 1719.
[60] M. Samiee, S. Konduri, B. Ganapathy, R. Kottokkaran, H. A. Abbas, A. Kitahara, P. Joshi, L. Zhang, M. Noack, V. Dalal, M. Samiee, S. Konduri, B. Ganapathy, R. Kottokkaran, *Appl. Phys. Lett.* **2014**, *105*, 153502.
[61] C. G. Shuttle, R. Hamilton, B. C. O'Regan, J. Nelson, J. R. Durrant, *Proc. Natl. Acad. Sci. USA* **2010**, *107*, 16448.
[62] J. Even, L. Pedesseau, J.-M. Jancu, C. Katan, *J. Phys. Chem. Lett.* **2013**, *4*, 2999.
[63] Z.-H. Wang, Y. Yang, L. Gu, H.-U. Habermeier, R.-C. Yu, T.-Y. Zhao, J.-R. Sun, B.-G. Shen, *Nanotechnology* **2012**, *23*, 265202.
[64] W. D. Dane, S. M. Vorpahl, S. D. Stranks, H. Nagaoka, G. E. Eperon, M. E. Ziffer, H. J. Snaith, D. S. Ginger, *Science* **2015**, *348*, 683.